# A Modular Medium Voltage Grid Connected Converter with Improved Switching Techniques for Solar Photovoltaic Systems

M. R. Islam, A. M. Mahfuz-Ur-Rahman, M. M. Islam, ***Y. G. Guo***, and J. G. Zhu

***Abstract*—The high-frequency common magnetic-link made of amorphous material, as a replacement for common dc-link, has been gaining considerable interest for the development of solar photovoltaic medium-voltage converters. Even though the common magnetic-link can almost maintain identical voltages at the secondary terminals, the power conversion system loses its modularity. Moreover, the development of high-capacity high-frequency inverter and power limit of the common magnetic-link due to leakage inductance are the main challenging issues. In this regard, a new concept of identical modular magnetic-links is proposed for high-power transmission and isolation between the low and the high voltage sides. Third harmonic injected sixty degree bus clamping pulse width modulation and third harmonic injected thirty degree bus clamping pulse width modulation techniques are proposed which show better frequency spectra as well as reduced switching loss. In this paper, precise loss estimation method is used to calculate switching and conduction losses of modular multilevel cascaded converter. To ensure the feasibility of the new concepts, a reduced size of 5 kVA rating, three-phase, five-level, 1.2 kV converter is designed with two 2.5 kVA identical high-frequency magnetic-links using Metglas magnetic alloy-based cores.**

***Index Terms*—Modular medium voltage converter, modular magnetic link, solar photovoltaic power plants, new modulation techniques, loss estimation.**

## I. Introduction

With the rapid development of large-scale solar photovoltaic (PV) power plants, the medium-voltage PV converter which enables solar PV power systems to be directly connected to the medium/high-voltage lines, without using heavy weight and large size line filters, boosters and step-up-transformers has become realistic [1]–[3]. In this emerging application, the modular multilevel cascaded (MMC) converter circuit topology has gained considerable popularity due to its superior features [4]–[7]. The requirement of isolated and balanced multiple dc supplies is the main drawback of MMC converter topology thereby its application is not always straightforward [8]. The H-bridge modules of the MMC converter associated with PV arrays may act as isolated dc sources and offer a new route to design medium-voltage multilevel converters [9]. On the other hand, the leakage currents due to the formation of stray capacitances between PV arrays and the ground is one of the major drawbacks, which may damage the PV arrays and introduce safety issues. High-frequency transformer-based isolated dc/dc converters are commonly used in MMC PV inverters to avoid the leakage currents and safety issues [10]. Asymmetrical multilevel converter requires multiple-imbalanced dc supplies. A method to create multiple-imbalanced sources for asymmetrical multilevel converter from a single source through a transformer was proposed in [11], where the dc power sources of the auxiliary modules are only supplied through the transformer. The dc power of the main module is supplied directly from the source, without ensuring any electrical isolation. Several papers in the literature proposed the use of common dc-link to minimize the voltage imbalance problem, e.g. a medium-voltage solar PV inverter with a common dc-link was proposed in [12]. Although these proposed topologies may lessen the voltage balancing issue, the creation of identical dc voltages from all PV arrays for the common dc-link complicates the system operation and limits the functionality of maximum power point tracker (MPPT). A high-frequency (about 10 kHz) common magnetic-link as a replacement for common dc-link was introduced in [13] to overcome the restriction of MPPT and complication of the PV inverter operation. The high-frequency common magnetic-link was used to generate multiple isolated and balanced power supplies from a single power supply. In [2], [3], a prototype 1 kV converter with a high-frequency common magnetic-link (as a replacement for common dc-link) was effectively utilized with solar PV and wind energy conversion system. However, the design and implementation of the high-power high-frequency inverter is considered as a tricky problem due to the unavailability of required semiconductor devices. Even though the proposed common magnetic-link as a replacement for common dc-link may overcome the voltage imbalance problem, the model lessens the modularity of the power conversion system. Modularity in the conversion system helps to increase the system reliability and reduce the cost, especially for high-power high-voltage applications. The leakage inductances generally limit the power handling capacity of the high-frequency transformers, and thereby it is critical to design a high-power system with a common

magnetic-link.

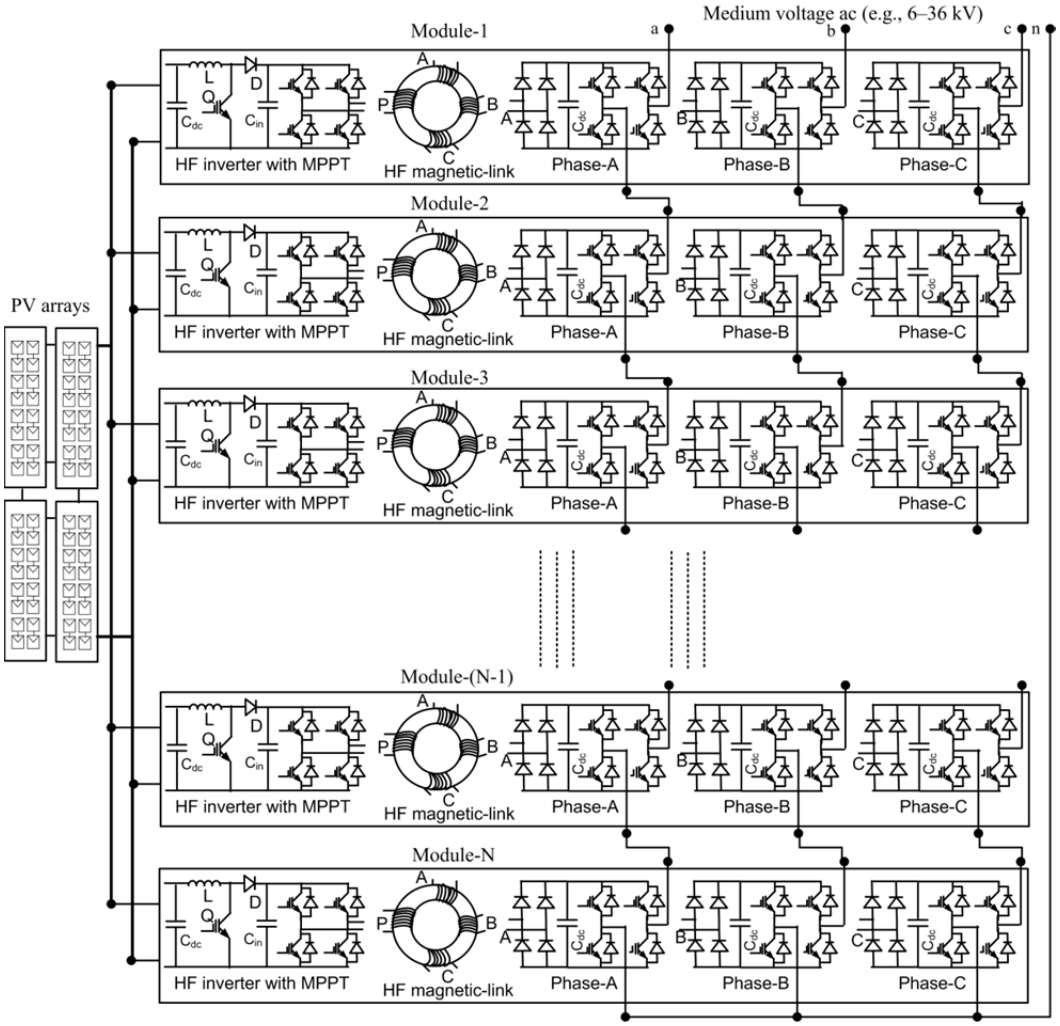


Fig. 1. Detailed circuit of the proposed totally modular medium-voltage PV converter with identical multiple four windings high-frequency magnetic-links

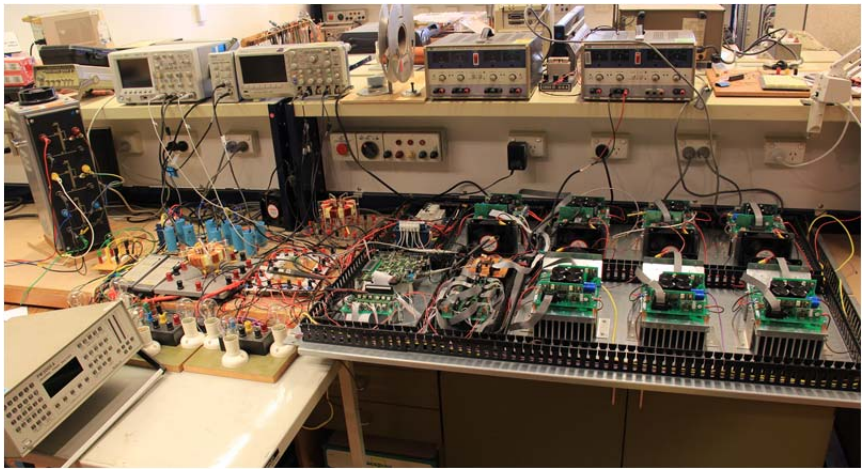

Fig. 2. Photograph of the test platform (1.2 kV system)

On the other hand, a number of identical four winding (a primary and three secondary windings) high-frequency magnetic-links can be used in parallel. The same source can be used to excite the primary windings of all magnetic-links. Fig. 1 illustrates the functional block diagram of the proposed modular medium-voltage PV converter. This paper presents the design and implementation of a novel medium-voltage converter with multiple identical four winding high-frequency magnetic-links. The amorphous alloy 2605S3A is chosen as

the core material because of its excellent electromagnetic characteristics [14], [15].

In the past decades, different types of pulse width modulation (PWM) techniques have been proposed, such as the sinusoidal pulse width modulation (SPWM), conventional space vector pulse width modulation (CSVPWM), third harmonic injected pulse width modulation (THPWM), trapezoidal pulse width modulation (TRPWM), sixty degree bus clamping pulse width modulation (SDBCPWM), and thirty degree bus clamping pulse width modulation (TDBCPWM). The performances of SPWM, THPWM and TRPWM were analysed and compared in [2]. The CSVPWM is considered a benchmark for pulse width modulation techniques [16]–[18]. Bus clamping PWM (BCPWM) methods are used to reduce the switching loss of the inverter [17], [18]. The BCPWM methods reduce harmonic distortion and pulsating torque in motor drives at high speeds [17], [18]. These techniques are also well employed in multi-level converters [19].

In this paper, the third harmonic injected sixty degree bus clamping pulse width modulation (THSDBCPWM) and third harmonic injected thirty degree bus clamping pulse width modulation (THTDBCPWM) techniques are proposed toimprove the frequency spectra and reduce the converter switching losses. A precise loss estimation method is used to calculate the switching and conduction losses of MMC converter under THSDBCPWM and THTDBCPWM using curve fitting and interpolation techniques. To assess the practical feasibility of the proposed new concepts, a prototype 5 kVA PV converter is developed with two 2.5 kVA identical amorphous alloy cores. Fig. 2 shows a photograph of the test platform. This eliminates the requirement for step-up-transformers to integrate solar PV systems into medium-voltage grids. The application of the transformer-less, compact, lightweight, and environmentally friendly direct integration technology will substantially reduce installation and maintenance costs and improve the system performance.

## II. Proposed Switching Techniques

### A. Traditional PWM

The commonly used modulation techniques are CSVPWM, SPWM, THPWM, SDBCPWM, TDBCPWM and TRPWM. The modulating signals of CSVPWM, SPWM, THPWM, SDBCPWM, TDBCPWM and TRPWM are shown in Fig. 3. In order to compare the performance of these modulation techniques, a three-phase, 15 levels, 11 kV MMC converter is modelled in MATLAB/Simulink environment. Fig. 4 depicts the output voltage waveforms of the MMC converter with six different modulation schemes with a carrier frequency of 4 kHz and modulation index of 1. In the modelling of switching controller, 14 level shifted in-phase disposition carriers (where all the carriers are in phase) are compared with the modulating signals and the corresponding gate pulses are produced for the insulated gate bipolar transistors (IGBTs). Level shifted carrier scheme shows better harmonic spectra than phase shifted scheme. Therefore, level shifted schemes are taken into consideration. The waveforms of the modulating signals from CSVPWM and THPWM schemes are quite similar. The CSVPWM scheme gives slightly better harmonics performance than that of THPWM. The modulating signals of SDBCPWM, TDBCPWM and TRPWM schemes have similar flattened top which helps to minimize switching loss. Among these three modulation schemes, the SDBCPWM and TDBCPWM schemes give almost the same total harmonic distortion (THD) of about 4.6%, which is much better than that of TRPWM scheme and complies with the IEEE1547 and IEC61727 standards. About 6.8% THD is calculated with TRPWM, which is also much higher than that obtained from SPWM scheme. Fig. 5 shows the harmonic spectrums of output voltage with different conventional modulation schemes. According to the harmonic performance and switching loss, the THPWM, SDBCPWM and TDBCPWM schemes have been considered for further investigation to introduce new modulation techniques.

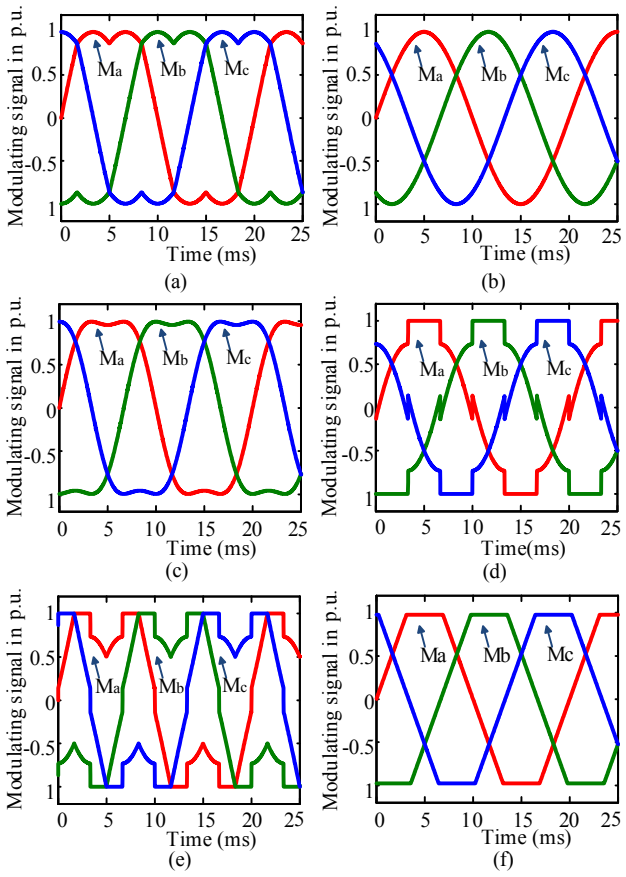


Fig. 3. Modulating signals corresponding to (a) CVSPWM, (b) SPWM, (c) THPWM, (d) SDBCPWM, (e) TDBCPWM, and (f) TRPWM

### B. Proposed Third Harmonic Injected Bus Clamping PWM

Two new modulation schemes, i.e. THSDBCPWM and THTDBCPWM, have been proposed based on THPWM, SDBCPWM and TDBCPWM schemes. The modulating signals of THSDBCPWM and THTDBCPWM schemes are shown in Fig. 6. In the proposed THSDBCPWM and THTDBCPWM modulation schemes, the modulating signals are flattened for sixty degree per half cycle and thirty degree per quarter cycle, respectively. During the flattened top interval no new gate pulses are generated for the switching devices.

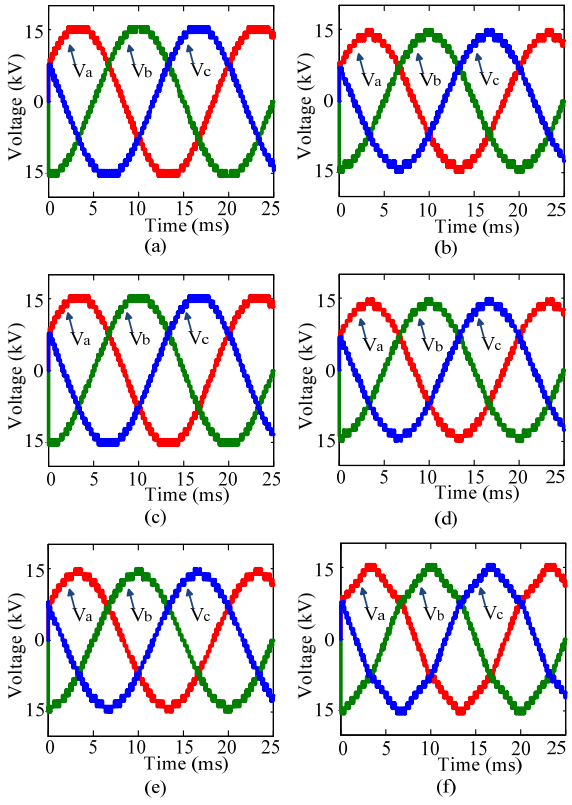


Fig. 4. Output line voltages corresponding to (a) CVSPWM, (b) SPWM, (c) THPWM, (d) SDBCPWM, (e) TDBCPWM, and (f) TRPWM

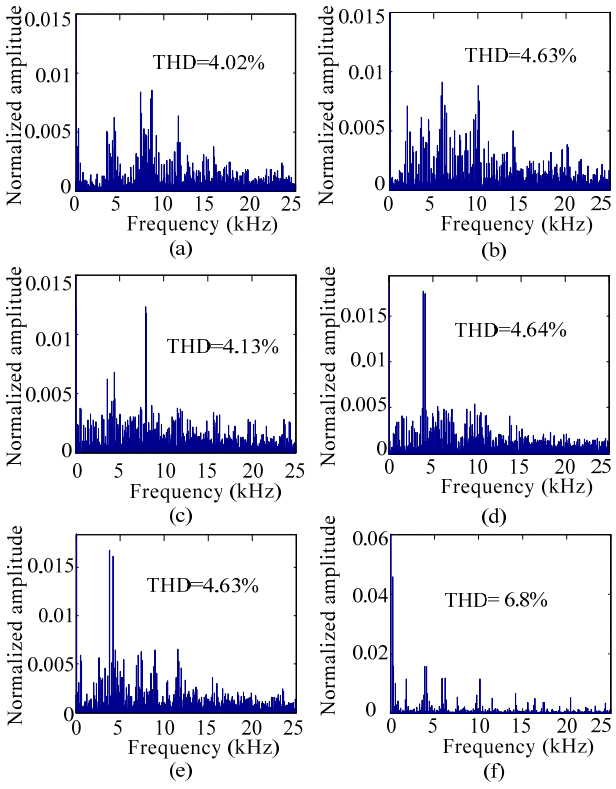


Fig. 5. Frequency spectrums of output voltage with modulation schemes (a) CVSPWM, (b) SPWM, (c) THPWM, (d) SDBCPWM, (e) TDBCPWM, and (f) TRPWM.

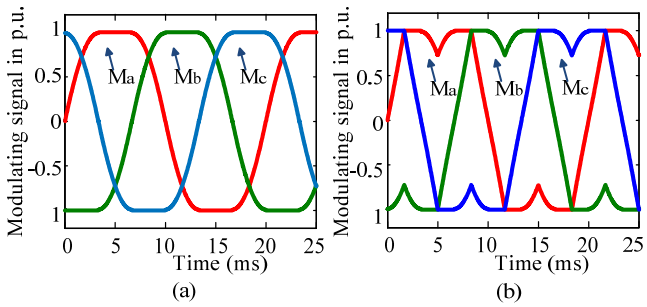


Fig. 6. Modulating signal of scheme: (a) THSDBCPWM, (b) THTDBCPWM

There are two states during the flattened top intervals:

- The modulating signal is greater than or equal to the carrier signal;
- The modulating signal is less than the carrier signal.

In both states, the corresponding switching devices remain on or off, which ensures no switching loss and involves only conduction losses.

For three phase inverters, three sine modulating signals are:

$$M_{a1} = A_m \sin(\omega t) \tag{1}$$

$$M_{b1} = A_m \sin(\omega t - 120^0) \tag{2}$$

$$M_{c1} = A_m \sin(\omega t + 120^0) \tag{3}$$

In case of third harmonic injected bus clamping PWM (THBCPWM), a common mode signal can be constructed from the third harmonic injected modulating signal. The common mode signal of THPWM, that has a frequency three times the fundamental frequency and a magnitude of $k$ times the fundamental amplitude, is added to the modulating signals in (1)–(3) to form the following new modulation signals

$$M_{a2} = A_m \sin(\omega t) + k \sin(3\omega t) \tag{4}$$

$$M_{b2} = A_m \sin(\omega t - 120^0) + k \sin(3\omega t) \tag{5}$$

$$M_{c2} = A_m \sin(\omega t + 120^0) + k \sin(3\omega t) \tag{6}$$

For bus clamping of the third harmonic injected signal, the following two common mode signals are required:

$$V_{cm1} = V_c - max(M_{a2}, M_{b2}, M_{c2}) \tag{7}$$

and

$$V_{cm2} = -V_c - min(M_{a2}, M_{b2}, M_{c2}) \tag{8}$$

where $V_c$ is the peak value of the carrier signal. By taking the combination of $V_{cm1}$ and $V_{cm2}$, different types of bus clamping PWM are possible. For THSDBCPWM, the common mode signal is formed by taking first sixty degree of $V_{cm2}$ and next sixty degree of $V_{cm1}$ and doing this in a periodic manner. But for THTDBCPWM, the common mode signal is formed in a reverse manner of THSDBCPWM, i.e. first $V_{cm1}$ is taken for sixty degree and then $V_{cm2}$ for the next sixty degree in a periodic manner. The common mode signal can easily be formed by multiplying a periodic function of each $V_{cm1}$ and $V_{cm2}$ and finally adding together. Fig. 7 shows the common mode signals of the proposed modulation schemes. The $f_1(\alpha)$ and $f_2(\alpha)$ are periodic functions of $\alpha$ and can be defined as

$f_1(\alpha)=0$ when $0^0<\alpha<60^0$

$=1$ when $60^0<\alpha<120^0$

and

$f_2(\alpha)=1$ when $0^0<\alpha<60^0$

$=0$ when $60^0<\alpha<120^0$

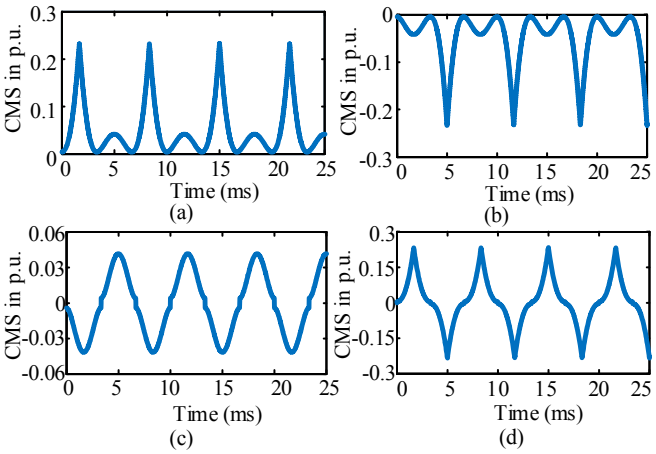


Fig. 7. Common mode signal corresponding to: (a) $V_{cm1}$, (b) $V_{cm2}$, (c) THSDBCPWM, and (d) THTDBCPWM.

Fig. 8 shows the output line voltages of the proposed converter with THSDBCPWM and THTDBCPWM modulation schemes. The THDs for the proposed THSDBCPWM and THTDBCPWM are 4.12% and 3.97%, respectively, as depicted in Fig. 9. The proposed THTDBCPWM scheme gives the best harmonic performance among all modulation schemes. Fig. 10 shows the flow chart to generate modulating signals of the proposed modulation schemes. Fig. 11 shows the THD versus modulating index bar graph for the proposed and conventional modulation schemes.

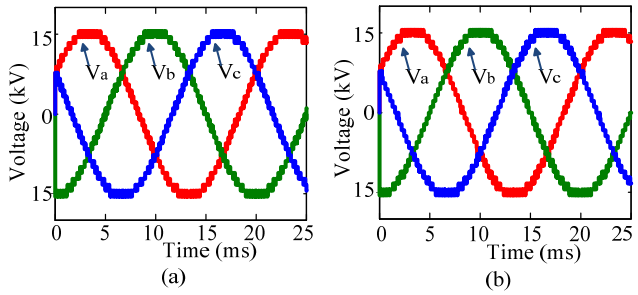


Fig. 8. Output line voltages of the proposed converter with modulation scheme: (a) THSDBCPWM and (b) THTDBCPWM.

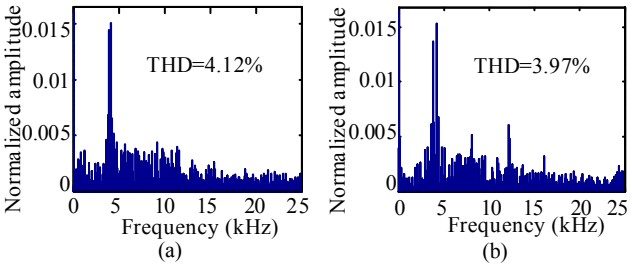


Fig. 9. Frequency spectrums of the output voltages with modulation scheme: (a) THSDBCPWM and (b) THTDBCPWM.

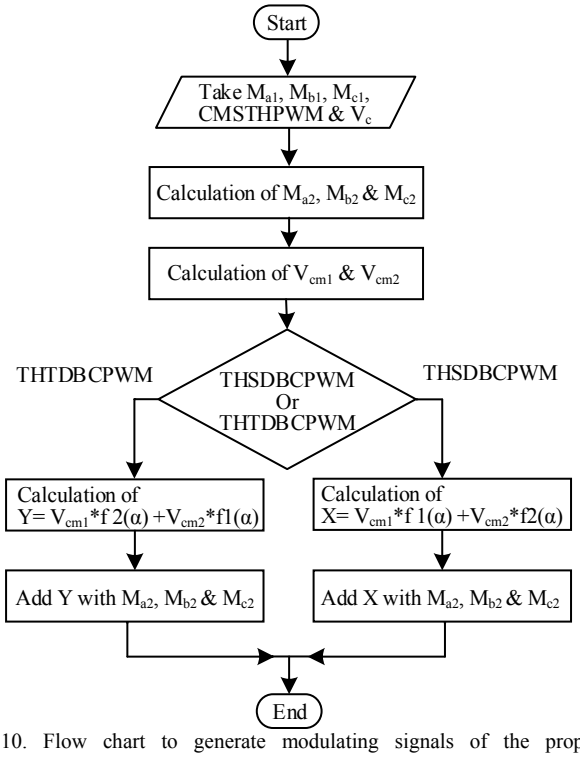


Fig. 10. Flow chart to generate modulating signals of the proposed THSDBCPWM and THTDBCPWM schemes.

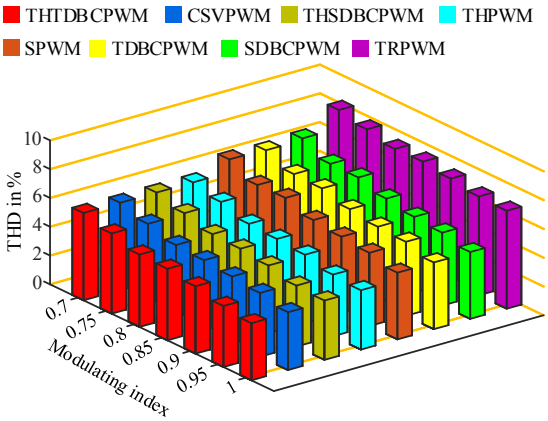


Fig. 11. THD versus modulating index for different modulation schemes.

### C. *Analysis of Switching and Conduction Losses of the Proposed Switching Schemes*

To analyse the loss performance of the proposed modulation schemes for a 15 level, 11 kV MMC converter, a commercially available IGBT module 5SNA1500E250300 is considered from ASEA Brown Boveri (ABB), whose voltage and current ratings are 2.5 kV and 1,500 A, respectively. In this paper, a precise loss estimation method is considered, which involves curve fitting and interpolation technique based on measured voltage and current waveforms. During the conduction mode, the IGBT collector-emitter voltage drop, $v_{ce}$ can be approximated as [20]

$$v_{ce} = v_{ce0} + R_c i_c \tag{9}$$

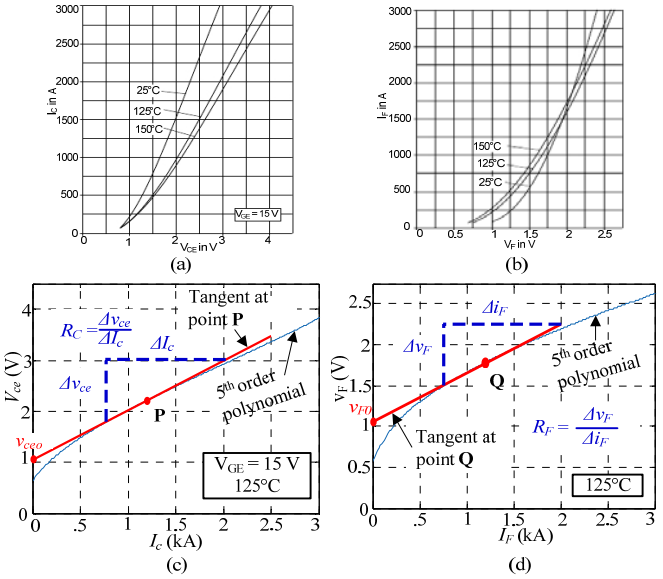


Fig. 12. (a) typical IGBT on-state characteristics, (b) typical diode forward characteristics from data sheet, (c) obtaining $v_{ceo}$ and $R_c$ from polynomial equation for IGBT and (d) obtaining $v_{Fo}$ and $R_F$ for diode.

where $v_{ce0}$ is the on-state zero-current collector-emitter forward voltage drop, and $R_c$ the collector emitter on-state resistance. For anti-parallel diodes, the voltage drop can be calculated as [20]:

$$v_F = v_{F0} + R_F i_F \tag{10}$$

where $v_{F0}$ is the on-state zero-current forward voltage drop and $R_F$ the on-state resistance. The parameters $v_{ceo}$, $R_c$, and $R_F$ ,can be obtained from the device datasheet. Fig. 12(a) shows the on-state characteristics of IGBT module 5SNA1500E250300 collected from the data sheet. The on-state characteristics at 125° C is considered for this study.

In MATLAB software environment, the pixel wise gray scale image processing and curve-fitting tool are used to deduce the 5th order polynomial equation of on-state characteristics of IGBT as:

$$v_{ce} = S_1 i_c^5 + S_2 i_c^4 + S_3 i_c^3 + S_4 i_c^2 + S_5 i_c + S_6 \tag{11}$$

where

$S_1 = 2.235\times10^{-17}$; $S_2 = -1.996\times10^{-13}$ ; $S_3 = 7.118\times10^{-10}$;
$S_4 = -1.294\times10^{-06}$; $S_5 = 0.002105$; *and* $S_6 = 0.6739$

Fig. 12(c) depicts the polynomial equation (11). The slope of the tangent at point P($i_{c1}, v_{ce1}$ ) can be deduced as:

$$\frac{dv_{ce}}{di_c} = S_1 i_c^4 + S_2 i_c^3 + S_3 i_c^2 + S_4 i_c^1 + S_5 = m_1 \tag{12}$$

when $i_c = i_{c1}$, then $m_1 = R_c$ and the zero-current collector–emitter forward voltage can be represent as:

$$v_{ce0} = v_{ce1} - (m_1 \times i_{c1}) \tag{13}$$

By using the polynomial equation to fit the diode forward characteristics (as shown in Fig. 12(b)), $v_F$ can also be obtained using the pixel wise gray scale image processing and curve-fitting tool as:

$$v_F = D_1 i_F^5 + D_2 i_F^4 + D_3 i_F^3 + D_4 i_F^2 + D_5 i_F + D_6 \tag{14}$$

where

$D_1 = 3.298\times10^{-17}$; $D_2 = -2.907\times10^{-13}$ ; $D_3 = 9.866\times10^{-10}$
$D_4 = -1.669\times10^{-06}$; $D_5 = 0.001975$; and $D_6 = 0.6265$.

Fig. 12(d) depicts the polynomial equation (14). At point Q($i_{F1}, v_{F1}$ )

$$R_F = \frac{dv_{ce}}{di_c}_{(i_c = i_{c1})} = m_2 \tag{15}$$

and

$$v_{F0} = v_{F1} - (m_1 i_{F1}) \tag{16}$$

The instantaneous IGBT conduction losses can be found as:

$$p_{cs}(t) = v_{ce}(t) i_c(t) = v_{ceo}(t) i_c(t) + R_c i_c^2 \tag{17}$$

and the average conduction loss can be calculated from [??]:

$$P_{ct} = \frac{1}{2\pi}\int_0^{2\pi} [p_{cs}(t)] d(\omega t) = \frac{1}{2\pi}\int_0^{2\pi} [v_{ceo}(t) i_c(t) + R_c i_c^2]\, d(\omega t) \tag{18}$$

$$P_{ct} = v_{ceo} I_{c,avg} + R_c I_{c,rms}^2 \tag{19}$$

where $I_{c,avg}$ and $I_{c,rms}^2$ are the average and rms currents of IGBT, respectively.

Similarly, the average diode conduction loss ($P_{cd}$) is:

$$P_{cd} = v_{F0} I_{F,avg} + R_F I_{F,rms}^2 \tag{20}$$

The total conduction loss per phase with $N$ IGBT switches can be expressed as:

$$P_{cond/phase} = \sum_{n=1}^{N} [\, P_{ct}(n) + P_{cd}(n)\, ] \tag{21}$$

Both switching losses ($E_{on}$ & $E_{off}$) are proportional to the switching frequency and blocking voltage across the IGBTs. The image processing based the 5th order polynomial equation of switching energy $(E_{on}, E_{off})$ can be represented as follows:

$$E_{on} = a_1 i_c^5 + a_2 i_c^4 + a_3 i_c^3 + a_4 i_c^2 + a_5 i_c + a_6 \tag{22}$$

$$E_{off} = b_1 i_c^5 + b_2 i_c^4 + b_3 i_c^3 + b_4 i_c^2 + b_5 i_c + b_6 \tag{23}$$

where

$a_1 = -1.217\times10^{-25}$ $b_1 = 4.309\times10^{-19}$
$a_2 = 8.32\times10^{-22}$ $b_2 = -3.189\times10^{-15}$
$a_3 = 5.391\times10^{-11}$ $b_3 = 1.445\times10^{-10}$
$a_4 = 2.552\times10^{-8}$ $b_4 = -6.775\times10^{-7}$
$a_5 = 0.000738$ $b_5 = 0.002042$
$a_6 = 0.09619$ $b_6 = 0.2036$

The polynomial equation of reverse recovery characteristics of diode at the junction temperature 125 °C, can be expressed as:

$$E_{rr} = c_1 i_F^5 + c_2 i_F^4 + c_3 i_F^3 + c_4 i_F^2 + c_5 i_F + c_6 \tag{24}$$

where

$c_1 = -2.34\times10^{-24}$; $c_2 = 3.211\times10^{-20}$; $c_3 = 5.448\times10^{-8}$
$c_4 = -0.0004056$; $c_5 = 1.108$; *and* $c_6 = 127.3$

The IGBT & diode switching power loss ($P_{swt}$ & $P_{rrd}$) for the fundamental period $T_o$ can be expressed as follows [21]:

$$P_{swt} = \frac{1}{T_o}\frac{V_{dc(min)}}{V_{dc(nom)}}\sum_{j=1}^{N}\left(E_{on_j}(i_c) + E_{off_j}(i_c)\right) \tag{25}$$

$$P_{rrd} = \frac{1}{T_o}\frac{V_{dc(min)}}{V_{dc(nom)}}\sum_{j=1}^{N}\left(E_{rrr_j}(i_F)\right) \tag{26}$$

where $V_{dc(min)}$ and $V_{dc(nom)}$ are the minimum and nominal dc-link voltage of each H-bridge inverter cell, respectively.

Based on the above equations, the converter switching and conduction losses are calculated and very impressive results are found. Fig. 13 shows different loss components, and Fig. 14 the loss performance of different modulation schemes. As shown, the proposed THSDBCPWM scheme has the lowest switching loss.

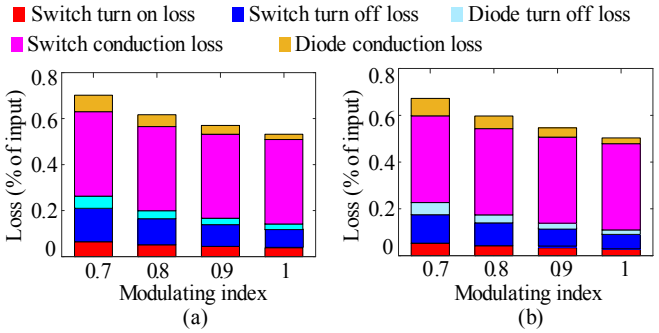


Fig. 13. Losses corresponding to (a) THTDBCPWM and (b) THSDBCPWM


Fig. 14. Switching loss of different modulation schemes.

## III. Amorphous High-Frequency Magnetic-Link

The first commercial amorphous soft magnetic material in the world is Metglas produced by Hitachi Metals Ltd. Even though nanocrystalline core shows reasonably lesser specific core losses than Metglas, the saturation flux density of nanocrystalline core (1.2 T) is much lower than that of Metglas (1.56 T). The magnetic alloys 2605SA1 and 2605S3A are two iron-based materials having saturation flux density of 1.56 T and 1.41 T, respectively. At 100 kHz sinusoidal voltage excitation of 0.2 T, the specific core loss of alloys 2605SA1 and 2605S3A are 600 W/kg and 100 W/kg, respectively. Recently, the market price of iron-based Metglas magnetic material has decreased significantly. For high-frequency applications, it is preferred to use a core material having high saturation flux density and low core loss to achieve compact, lightweight and efficient system.

Because of these superior characteristics (higher saturation flux density and lower specific core loss), market cost, and availability of various size strips (width) the Fe-based amorphous magnetic alloy 2605S3A has been chosen as the core material [14], [15].

A five-level three-phase inverter requires two modules, each of which requires three isolated and balanced dc sources. Each link comprises a primary and three secondary windings for the three-phases of the module. Based on the optimization results, 2 kg amorphous alloy 2605S3A sheet (2.5 cm wide and 20 μm thick) was acquired from Metglas Metals Inc., USA. A core manufacturing platform was created in the laboratory for proper wrapping of μm thickness sheets, as shown in Fig. 15. Araldite 2011 was applied on the surface of each layer of Metglas sheet to ensure electrical insulation and mechanical bonding. During the entire wrapping of Metglas stripes of 2605S3A, a tensive force was applied to spread the glue, i.e. Araldite 2011 uniformly on the surface of Metglas sheet. After wrapping, the frames were removed before the Araldite dried up, in about 2 hours. Litz wires were used in windings with single layer placement only, which can effectively minimize the proximity effect. Fig. 16 shows a photograph of two identical modular high-frequency magnetic-links for two modules of the prototype five-level converter.

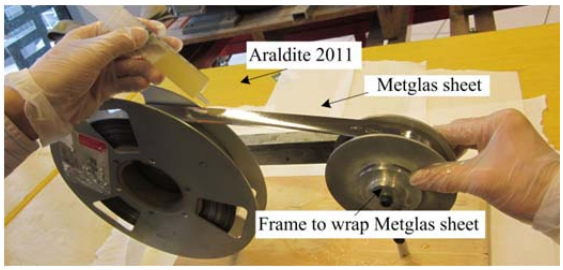


Fig. 15. Photographs of Metglas sheet wrapping process to develop a core.

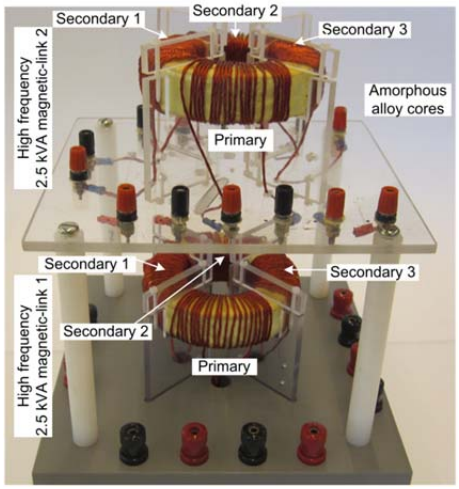


Fig. 16. A photograph of the prototype 5 kVA high-frequency magnetic-link with two identical 2.5 kVA cores

## IV. Experimental Validation

In the proposed converter, each module includes an inverter circuit with an MPPT, a magnetic-link, and rectifier-inverter sets. A module can generate three line voltage levels when measuring between lines. The power level of the proposed converter can be readily changed by adding or removing some identical modules. The dc-power available from the solar PV arrays is converted into high-frequency ac by the high-frequency inverters to energize the primary windings of the high-frequency magnetic-links. Bridge rectifiers are used to convert the high-frequency ac-power (from the secondary windings) into dc-power to supply an H-bridge cell as an isolated dc-supply.

To validate the practicality of the proposed completely modular medium voltage inverter with identical multiple four windings high-frequency magnetic-links, a scaled down prototype test platform of 5 kVA rating, 1.2 kV, 5-level 3-phase converter system is developed. The proposed THSDBCPWM and THTDBCPWM modulation schemes are used to model the switching controller of the proposed converter. The dc solar power from 400 V PV array is converted into 6 kHz square-wave ac by the high-frequency inverter and is used to energize the primary winding of the magnetic-link. The excitation voltage and current and secondary induced voltage waveforms are shown in Fig. 17(a) and in Fig. 17(c). The output from each secondary winding is connected to a rectifier circuit made of fast recovery diodes and followed by a low pass RC filter circuit. The compact IGBT module SK30GH123 and isolated drive SKHI 20opA are used to prototype H-bridge cells and high-frequency inverters in the laboratory. Fig. 17(b) shows the gate pulses of a particular H-bridge cell. The output phase and phase current are measured, as depicted in Fig. 17(d). The output voltage waveforms comprise a number of voltage levels in which each voltage level is constituted by many PWM pulses. The line to line voltage of the prototype converter is shown in Fig. 17(e), with THD of 15%. In order to reduce the THD to a level less than 5% to comply with the IEEE1547 and IEC61727 standards, an LC filter circuit was used. As measured, after the line filter circuit, the output line-to-line voltage waveform contains less than 4% THD, as shown in Fig. 17(f). The losses of the prototype inverter were measured and the overall efficiency was found to be 78% which is about 12–15% lower than the traditional two-level PV inverter.

However, the traditional two-level inverter based grid connected PV system employs step-up-transformer which along with the line filter is responsible for up to 50% of the total system losses [22]. Using the proposed medium-voltage modular PV inverter, it is possible to interconnect the solar PV system to medium voltage grid without using a step-up-transformer and harmonic neutralization filter. The elimination of heavy and large size step-up-transformer and line filter may help improve the system performance and reduce the cost of installation, running, and maintenance.

## V. Conclusion

A totally modular medium-voltage converter has been proposed in this paper for solar PV power plants. Multiple identical four windings low-power magnetic cores as a replacement for the common high-power core have been used, which ensures the system modularity and significantly lessens the core leakage inductances. Although the additional power conversion stage and high-frequency magnetic-links may add considerable losses to the system, still the overall performance is comparable with the traditional step-up-transformer and line filter-based system. However, the line filter and step-up-transformer less grid integration will enable large savings in system cost. This paper has also introduced two new modulation schemes, i.e. THSDBCPWM and THTDBCPWM. The proposed modulation schemes can provide the lowest THD and switching loses compared with the conventional schemes. The proposed modulation schemes can also be applicable for other power converter circuits.

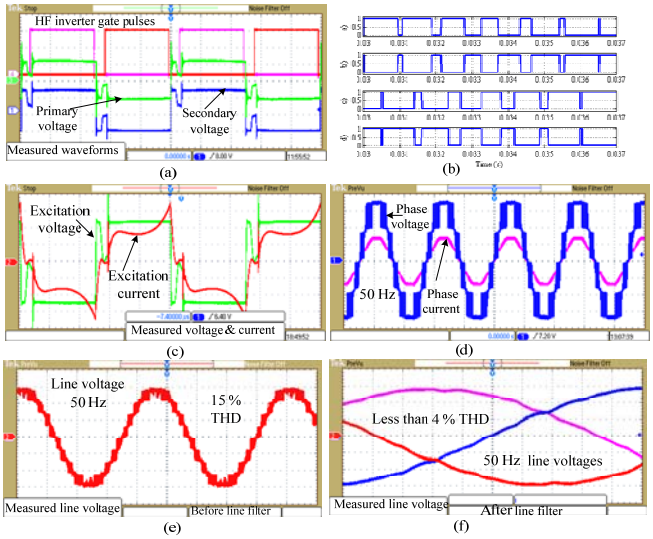


Fig. 17. Measured waveforms of the prototype inverter: (a) gate pulses for the high-frequency (HF) inverter and primary/secondary voltage of the magnetic-link, (b) gate pulses for a particular H-bridge cell, (c) excitation voltage and current of the magnetic-link, (d) phase voltage and current of the proposed converter with THSDBCPWM, (e) line to line voltage; before line filter circuit, and (f) three line to line voltage (zoom factor is 6); after LC filter.

## References


[1] S. A. Azmi, G. P. Adam, K. H. Ahmed, S. J. Finney, and B. W. Williams, "Grid interfacing of multimegawatt photovoltaic inverters," *IEEE Trans. Power Electron.,* vol. 28, no. 6, pp. 2770–2784, June 2013.

[2] M. R. Islam, Y. G. Guo, and J. G. Zhu, "A high-frequency link multilevel cascaded medium-voltage converter for direct grid integration of renewable energy systems," *IEEE Trans. Power Electron*., vol. 29, no. 8, pp. 4167–4182, Aug. 2014.

[3] M. R. Islam, Y. G. Guo, and J. G. Zhu, "A multilevel medium-voltage inverter for step-up-transformer-less grid connection of photovoltaic power plants," *IEEE J. Photovoltaics*, vol. 4, no. 3, pp. 881–889, May 2014.

[4] B. P. McGrath, D. G. Holmes, and W. Y. Kong, "A decentralized controller architecture for a cascaded H-bridge multilevel converter," *IEEE Trans. Ind. Electron.*, vol. 61, no. 3, pp. 1169–1178, March 2014.

[5] E. Babaei, S. Laali, and S. Alilu, "Cascaded multilevel inverter with series connection of novel H-bridge basic units," *IEEE Trans. Ind. Electron.*, vol. 61, no. 12, pp. 6664–6671, Dec. 2014.

[6] C. Buccella, C. Cecati, M. G. Cimoroni, and K. Razi, "Analytical method for pattern generation in five-level cascaded H-bridge inverter using selective harmonic elimination," *IEEE Trans. Ind. Electron.*, vol. 61, no. 11, pp. 5811–5819, Nov. 2014.

[7] S. K. Chattopadhyay, and C. Chakraborty, "A new multilevel inverter topology with self-balancing level doubling network," *IEEE Trans. Ind. Electron.*, vol. 61, no. 9, pp. 4622–4631, Sept. 2014.

[8] F. Deng and Z. Chen, "Voltage-balancing method for modular multilevel converters under phase-shifted carrier-based pulsewidth modulation," *IEEE Trans. Ind. Electron.,* vol. 62, no. 7, pp. 4158–69, 2015.

[9] B. Xiao, L. Hang, J. Mei, C. Riley, L. M. Tolbert, and B. Ozpineci, "Modular cascaded H-bridge multilevel PV inverter with distributed MPPT for grid-connected applications," *IEEE Trans. Ind. Applicat.*, vol. 51, no. 2, pp. 1722–1731, 2015.

[10] F. F. Edwin, W. Xiao, and V. Khadkikar, "Dynamic modeling and control of interleaved flyback module-integrated converter for PV power applications," *IEEE Trans. Ind. Electron.*, vol. 61, no. 3, pp. 1377–1388, 2014.

[11] J. Pereda and J. Dixon, "High-frequency link: a solution for using only one dc sources in asymmetric cascaded multilevel inverters," *IEEE Trans. Ind. Electron.*, vol. 58, no. 9, pp. 3884–3892, 2011.

[12] S. Kouro, C. Fuentes, M. Perez, and J. Rodriguez, "Single dc-link cascaded H-bridge multilevel multistring photovoltaic energy conversion system with inherent balanced operation," in *Proc. 38th Ann. Conf. IEEE Ind. Electron. Soc. (IECON2012)*, Canada, 25–28 Oct. 2012, pp. 4998–5005.

[13] M. R. Islam, Y. G. Guo, and J. G. Zhu "A medium frequency transformer with multiple secondary windings for medium voltage converter based wind turbine power generating systems," *J. Appl. Phys.*, vol. 113, no. 17, art. 17A324, 2013.

[14] D. Azuma and R. Hasegawa, "Core loss in toroidal cores based on Fe-based amorphous Metglas 2605HB1 alloy," *IEEE Trans. Magn.*, vol. 47, no. 10, pp. 3460–3462, 2011.

[15] T. Fan, Q. Li, and X. Wen, "Development of a high power density motor made of Amorphous alloy cores," *IEEE Trans. Ind. Electron.*, vol. 61, no. 9, pp. 4510–4518, 2014.

[16] A. Ruiz-Gonzalez, M. J. Meco-Gutierrez, F. Perez-Hidalgo, F. Vargas-Merino, and J. R. Heredia-Larrubia, "Reducing acoustic noise radiated by inverter-fed induction motors controlled by a new PWM strategy," *IEEE Trans. Ind. Electron.*, vol. 57, no. 1, pp. 228–236, Jan. 2010.

[17] V. S. S. P. K. Hari and G. Narayanan, "Space-vector based hybrid pulse width modulation technique to reduce line current distortion in induction motor drives," *IET Power Electron.*, vol. 5, no. 8, pp. 1463–1471, 2012.

[18] K. Basu, J. S. S. Prasad, and G. Narayanan, "Minimization of torque ripple in PWM AC drives," *IEEE Trans. Ind. Electron.*, vol. 56, no. 2, pp. 553–558, Feb. 2009.

[19] Z. Zhang, O. C. Thomsen, and M. A. E. Anderson, "Discontinuous PWM modulation strategy with circuit-level decoupling concept of three-level neutral-point-clamped inverter," *IEEE Trans. Ind. Electron.*, vol. 60, no. 5, pp. 1897–1906, May 2013.

[20] C. D. Townsend, T. J. Summers, J. Vodden, and *et al.,* "Optimization of switching losses and capacitor voltage ripple using model predictive control of a cascaded H-bridge multilevel StatCom," *IEEE Trans. Power Electron*., vol. 28, no. 7, pp 3077–3087, Jul. 2013.

[21] T. Brückner and S. Bernet, "Estimation and measurement of junction temperatures in a three-level voltage source converter," *IEEE Trans. Power Electron.*, vol. 22, no. 1, pp. 3–12, 2007.

[22] F. Z. Peng, J. S. Lai, J. W. McKeever, and J. V. Coevering, "A multilevel voltage–source inverter with separated dc sources for static var generation," *IEEE Trans. Ind. App.*, vol. 32, no. 5, pp. 1130–1138, 1996.

[23]